

Nodal frequency-constrained energy storage planning via hybrid data-model driven methods

Jiaxin Wang¹, Jiawei Zhang² , Min Yang¹, Yating Wang² and Ning Zhang¹

ABSTRACT

Cross-regional high voltage direct current (HVDC) systems bring remarkable renewable power injections to the receiver side of power grids. However, HVDC failures result in large disturbances to receivers and cause critical frequency security problems. High renewable energy penetration also reduces the system inertia and damping coefficients. Thus, some nodal frequency nadirs may be much lower than those calculated by the center-of-inertia (COI) and may trigger low-frequency protection. Energy storage is a promising solution for frequency-related problems. In this study, we build an energy storage planning model considering both COI and nodal frequency security constraints. The energy storage capacities and locations are determined in the planning scheme based on year-round operations. First, we carry out a year-round COI-frequency-constrained unit commitment to obtain comprehensive operation modes. Next, we propose a hybrid data-model driven approach to generate nodal frequency security constraints for extensive operation modes effectively. Finally, we achieve optimal energy storage planning with both COI and nodal frequency constraints. Case studies on a modified RTS-79 test system and a 1089-bus power system in practical in Jiangsu, China, verify the effectiveness of the proposed methods.

KEYWORDS

Frequency nadir, energy storage, inverter-based resources, security-constrained planning.

High renewable energy penetration has become an essential feature of power systems. The replacement of conventional units with renewable energy resources reduces the system inertia. The resulting low inertia characteristic poses risks to frequency security, raising concerns among system operators and engineers. Moreover, large-scale cross-regional high voltage direct currents (HVDCs) are popular in regions with uneven spatial distributions of renewable resources and power loads. For example, China is planning and running more than twenty ± 800 kV and ± 1100 kV HVDC transmission lines, each carrying 8–10 GW of active power^[1,2]. Brazil uses ± 800 kV HVDC systems to transmit 8 GW of power from hydropower plants in Belo Monte to load centers 2000 kilometers away^[3]. The large disturbances caused by HVDC blocking contingencies aggravate system frequency security risks, particularly under high renewable penetrations. Therefore, it is necessary and urgent to improve the frequency security of power systems in the near future.

Energy storage with frequency regulation is a promising solution to frequency security problems. First, energy storage systems can provide primary and secondary frequency regulation to improve the frequency dynamics of power systems^[4]. Second, many flexible control strategies have been developed for energy storage systems to respond quickly and effectively to frequency deviations^[5]. Third, while this topic is outside the scope of our paper, energy storage systems can also provide other ancillary services, such as peak shaving and voltage support, to improve the reliability of power systems^[6]. Finally, the investment cost of energy storage systems is decreasing, and their efficiency is increasing, which may make energy storage systems more competitive in the future^[7]. Thus, large-scale energy storage systems will need investment in the near future to ensure the frequency security of power systems. Deter-

mining where and how much energy storage should be placed to satisfy the frequency security requirements has become an urgent topic for power system planners.

Considering the frequency security requirements in mathematical constraints is a key challenge in energy storage planning. The frequency security requirements are usually composed of two components: the rate of change of frequency (RoCoF) requirements and frequency nadir requirements. The RoCoF requirements have simple linear forms, whereas the frequency nadir requirements are more complex. Previous studies have derived center-of-inertia (COI) frequency nadir constraints via multiple approaches. First, the constraints can be approximated through simplified frequency response models. For example, researchers assume that the power outputs of the primary regulation of conventional units are linearly correlated with time^[8,9]. Second, the piecewise linearization method combines model and data characteristics to construct mathematical constraints^[10,11]. Finally, data-driven approaches that use methods such as support vector machines^[12], classification trees^[13,14], and deep neural networks^[15,16] are also popular for extracting frequency security constraints. Data-driven methods are model friendly and can be applied to nonlinear industrial models. However, the COI frequency model neglects the spatial differences among power grid buses. As a result, it can only determine the capacity of energy storage devices but not their locations in planning models.

Some recent research has considered the grid structure and unit differences in frequency response models. A previous report revealed nodal frequency differences after disturbances in Nordic power systems^[17]. Researchers have studied interarea oscillations and mathematical models describing these phenomena^[18]. The swing equations considering power grids are derived and applied to virtual inertia placement problems to minimize the H_2 norm^[19].

¹Department of Electrical Engineering, Tsinghua University, Beijing 100084, China; ²China Electric Power Planning and Engineering Institute, Beijing 100120, China

Address correspondence to Jiawei Zhang, jw-zhang15@tsinghua.org.cn

Furthermore, a frequency divider formula is proposed to accurately estimate the nodal frequencies in transient processes^[20,21]. However, the nodal frequency nadir constraints have not been well studied in energy storage planning problems. In this work, we set both the COI and nodal frequency requirements in energy storage planning problems. The frequencies on all buses are limited to be above a set threshold after large disturbances. This approach can guarantee the frequency quality requirements of common power users, highlight nodal differences, and guide energy storage placements.

Another challenge in energy storage planning is addressing the complexity posed by extensive time horizons. The planning problems span long periods and must account for various operational modes^[22]. The vast number of time horizons complicates the generation of nodal frequency security constraints for each operational mode. Additionally, solving the overall planning problem becomes particularly time-consuming^[23]. The use of aggregations is a major approach for reducing computational challenges. The unit models and renewable time series are clustered to reduce decision variables in year-round problems^[23–25]. Representative days and system state models are also applied for energy storage planning^[26]. However, the aggregations may lose detailed information and lead to suboptimal solutions. Moreover, generating nodal frequency security constraints for each operational mode is still a challenge.

This paper provides solutions for energy storage planning, with a focus on incorporating nodal frequency security constraints. Figure 1 depicts the framework of the proposed method. First, we carry out a year-round COI-frequency-constrained unit commitment (UC) to obtain comprehensive operation modes. Second, we develop a hybrid data-model-driven approach to generate the nodal frequency constraints for each mode. Then, we formulate and efficiently solve a frequency-constrained energy storage planning optimization problem, where primary regulations, secondary regulations, and peak-shaving functions are also considered. Our methods are verified for a modified RTS-79 test case and a 1089-bus practical power system in Jiangsu, China. The results suggest that the proposed planning model can effectively determine the energy storage capacities and locations to satisfy both the COI and nodal frequency security requirements.

The major contributions are as follows.

- A hybrid data-model-driven approach is developed to generate nodal frequency security constraints for extensive operational modes effectively.
- A year-round energy storage planning model with COI and nodal frequency constraints is established for large-scale power systems. A case study on a 1089-bus power system from Jiangsu, China, verifies the efficiency and effectiveness of the proposed method.

The rest of the paper is organized as follows. Section 1 explains the framework of our methods and the main notations used in the paper. Section 2 introduces the year-round COI frequency-constrained UC model. Section 3 presents the hybrid data-model-driven approach to generate nodal frequency constraints. Section 4 formulates the final frequency-constrained energy storage planning model. Section 5 verifies the proposed method for a modified RTS-79 test case and a 1089-bus power system from Jiangsu, China.

1 Problem statement and our framework

1.1 Problem statement

We consider a transmission power system with n generator buses and n_d load buses. The indices of generator buses are denoted as $\mathcal{G} = \{1, 2, \dots, n\}$ and the indices of load buses are denoted as $\mathcal{L} = \{n+1, n+2, \dots, n+n_d\}$. The set of all buses is $\mathcal{N} = \mathcal{G} \cup \mathcal{L}$. The transmission lines are denoted by $\mathcal{B} \subset \mathcal{N} \times \mathcal{N}$. In such a transmission system, we aim to place some energy storage devices to improve the system's frequency security. A core problem is determining the locations and capacities of energy storage devices under some economic objectives and within frequency security constraints.

As outlined in the introduction, a planning model for energy storage placement should consider at least the following aspects: (1) The frequency support capabilities of both energy storage systems and traditional synchronous generators should be considered. (2) Security requirements for both nodal and center-of-inertia frequencies should be satisfied after predefined disturbances. (3) The scalability of large-scale power systems needs to be guaranteed.

1.2 Our framework

We formulate a year-round energy storage planning model with frequency security constraints. The objective is to minimize the total economic costs, as shown in Eq. (31). The complete constraints are composed of the following parts. The energy storage operational behaviors are formulated in constraints Eqs. (26)–(30). The synchronous generators' operational behaviors are formulated in constraints Eqs. (9)–(13), where binary variables are finally relaxed according to their operation modes. The power balance constraints are shown in Eq. (32). The center-of-inertia frequency security constraints are formulated as Eqs. (7) and (8). Nodal frequency security constraints are formulated as Eq. (21), which are generated through our proposed hybrid data-model driven approach.

The workflow of the proposed method is illustrated in Figure 1.

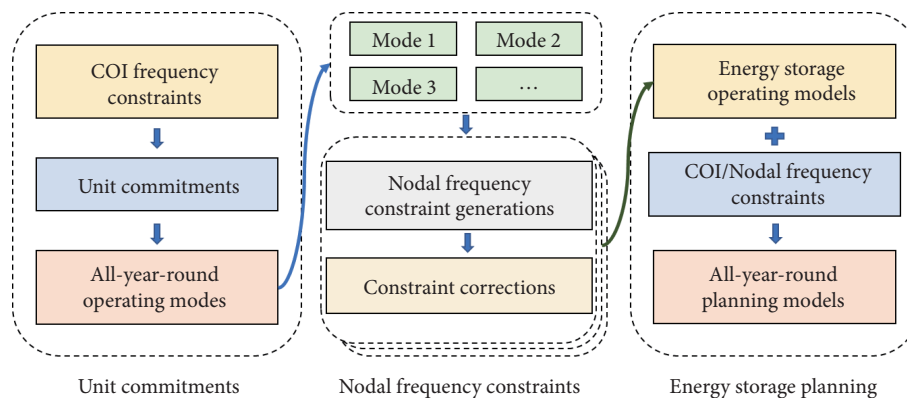


Figure 1 Framework of the proposed method.

For enhanced clarity, a comprehensive explanation of the workflow is provided. First, the center-of-inertia frequency security constraints are derived utilizing alternate support vector machine decision tree (ASVM-TREE) method (see Section 2.2). Second, these COI frequency security constraints are integrated into the year-round unit commitment model (see Section 2.3), resulting in a center-of-inertia frequency-constrained year-round unit commitment model. By solving this model, the power system's all-year operation modes are obtained (defined in Section 2.4). Third, the nodal frequency security constraints for each operation mode are generated through our proposed hybrid data-model driven approach (see Sections 3.3–3.5). Finally, we integrate the frequency security constraints into the energy storage planning model formulated in Section 5. A complete optimization problem (described in this section) is obtained and solved to determine the optimal energy storage placements.

1.3 Notations

We list the main notations used in the paper. The indices of generation-side buses are $\mathcal{G} = \{1, 2, \dots, n\}$, and the indices of load-side buses are $\mathcal{L} = \{n+1, n+2, \dots, n+n_d\}$. The set of all buses is $\mathcal{N} = \mathcal{G} \cup \mathcal{L}$. The set of all transmission lines is $\mathcal{B} \subset \mathcal{N} \times \mathcal{N}$. The possible locations of energy storage devices are $\mathcal{E} \subset \mathcal{L}$ and $\mathcal{E} = \mathcal{L}$ when we do not limit the locations. The time horizons are $\mathcal{T} = \{1, 2, \dots, N_T\}$, where N_T is the total number of hours considered in the optimization problem. The locations of the renewables are $\mathcal{R} \subset \mathcal{N}$, and the locations of the HVDC terminals are $\mathcal{H} \subset \mathcal{N}$. We use $|\cdot|$ to denote the cardinality of a set. For example, $|\mathcal{G}| = n$ and $|\mathcal{L}| = n_d$.

The inertia vector of the generators is $m = [m_i]_{i \in \mathcal{G}}$. The damping coefficient vector of the generators and loads are $d = [d_i]_{i \in \mathcal{G}}$ and $\mu = [\mu_i]_{i \in \mathcal{L}}$, respectively. The droop coefficient vector of the generators and energy storage devices are $\kappa = [\kappa_i]_{i \in \mathcal{G}}$ and $K = [K_i]_{i \in \mathcal{L}}$, respectively. We use $\text{diag}(\cdot)$ to denote a diagonal matrix with the input vector providing the diagonal elements of the matrix. For example, $M = \text{diag}(m)$ is the inertia matrix, and $D = \text{diag}(d)$ is the

damping coefficient matrix.

We use ω to denote the frequency deviation after disturbances. The generation-side frequency deviation vector is $\omega_{\mathcal{G}} = [\omega_i]_{i \in \mathcal{G}}$, and the load-side frequency deviation vector is $\omega_{\mathcal{L}} = [\omega_i]_{i \in \mathcal{L}}$. The relationship between $\omega_{\mathcal{G}}$ and $\omega_{\mathcal{L}}$ is given by

$$\omega_{\mathcal{L}} = F\omega_{\mathcal{G}}, \quad (1)$$

where F is the frequency divider matrix proposed in Ref. [20]. The generation-side power injection vector $P^{\mathcal{G}}$ and the load-side power injection vector $P^{\mathcal{L}}$ also have similar relationships, i.e.,

$$P^{\mathcal{G}} = LP^{\mathcal{L}}, \quad (2)$$

where L is the load power distribution matrix proposed in Ref. [27]. We can partition the admittance matrix B into four blocks as

$$B = \begin{bmatrix} B_{\mathcal{G}\mathcal{G}} & B_{\mathcal{G}\mathcal{L}} \\ B_{\mathcal{L}\mathcal{G}} & B_{\mathcal{L}\mathcal{L}} \end{bmatrix}. \quad (3)$$

Then, the frequency divider matrix $F = -B_{\mathcal{L}\mathcal{L}}^{-1}B_{\mathcal{L}\mathcal{G}}$ and the load power distribution matrix $L = B_{\mathcal{G}\mathcal{L}}B_{\mathcal{L}\mathcal{L}}^{-1}$.

2 Year-round COI frequency-constrained UC problem

2.1 Center-of-inertia frequency response model

Figure 2 shows the classical center-of-inertia frequency response model after disturbances. We consider seven kinds of typical conventional units, including coal-fired, gas-fired, and hydro units with different capacities and energy storage, in the frequency response model. All conventional units use industry-level models developed by the China Electric Power Research Institute^[28].

We denote the on-off status of the generators by x_g for $g \in \mathcal{G}$. The center-of-inertia droop coefficient of the generators is

$$\kappa^{\text{coi}} = \sum_{g \in \mathcal{G}} x_g \kappa_g. \quad (4)$$

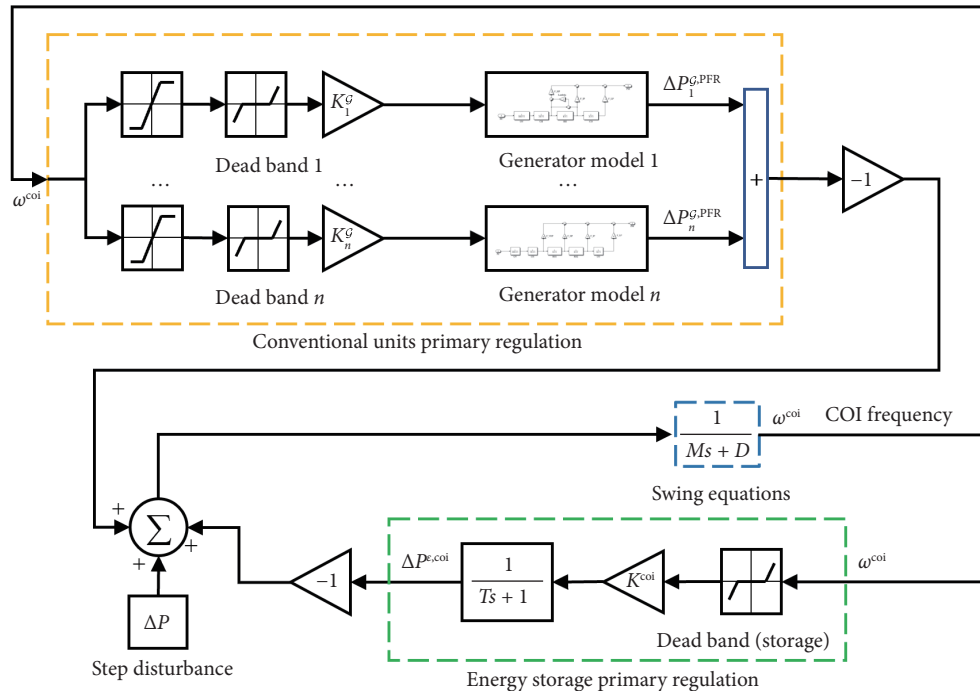


Figure 2 Center-of-inertia frequency response model.

The center-of-inertia damping and inertia are

$$d^{\text{coi}} = \sum_{g \in \mathcal{G}} x_g d_g + \sum_{i \in \mathcal{L}} \mu_i, \quad m^{\text{coi}} = \sum_{g \in \mathcal{G}} x_g m_g. \quad (5)$$

Energy storage provides the primary regulation $\Delta P^{\mathcal{E}, \text{coi}}$ in response to the center-of-inertia frequency deviation ω^{coi} , i.e.,

$$\Delta P^{\mathcal{E}, \text{coi}} = \frac{K^{\text{coi}}}{Ts + 1} \omega^{\text{coi}}, \quad (6)$$

where $K^{\text{coi}} = 1^T K$ is the sum of the droop coefficients of energy storage devices.

2.2 Data-driven COI frequency constraints

We should ensure that the power system's frequency RoCoF and nadir are within the required restrictions under the COI assumption.

The RoCoF constraint is shown in Eq. (7). r^{coi} is the RoCoF of the COI frequency, and ΔP^{coi} is the disturbance power.

$$r^{\text{coi}} = \frac{\Delta P^{\text{coi}}}{m^{\text{coi}}} \leq r^{\text{max}}, \quad (7)$$

where r^{max} is the maximum RoCoF limit and is set to 1 s/Hz in this paper.

We extract the COI frequency nadir constraints from massive simulations via the alternate support vector machine decision tree (ASVM-TREE) method^[14]. Figure 3 illustrates the ASVM-TREE method. It builds multiple linear cutting planes to classify whether the frequency nadir satisfies the requirement ($\omega^{\text{nadir}} \geq \omega_{\text{th}}$).

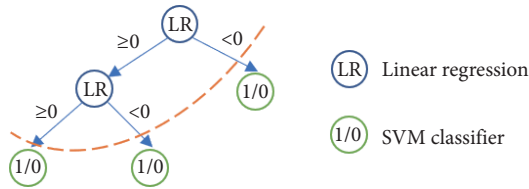


Figure 3 Alternate support vector machine decision tree (ASVM-TREE).

The extracted COI frequency nadir constraints take the form of Eq. (8). The variables in the constraints are the on-off status of the generators (x_g), the droop coefficient of energy storage (K^{coi}), and the power load ($P^{\mathcal{L}, \text{coi}}$). Notably, the value of the power load affects the frequency nadir through the load damping coefficient μ .

$$A[x_1, x_2, \dots, x_n, K^{\text{coi}}, P^{\mathcal{L}, \text{coi}}]^T + b \geq 0, \quad (8)$$

where A is a constant matrix and b is a constant vector. The inequality in Eq. (8) comprises multiple linear cutting planes, which are extracted from the ASVM-TREE.

2.3 Year-round unit commitment

The unit commitment (UC) constraints are composed of decision variable bound constraints, generator on-off status constraints, minimum startup and shutdown time constraints, and ramping constraints.

The bound constraints are as follows:

$$P_g^{\text{min}} x_{g,t} \leq P_g^{\mathcal{G}} \leq P_g^{\text{max}} x_{g,t}, \quad (9)$$

where P_g^{min} and P_g^{max} are the minimum and maximum power outputs of generator $g \in \mathcal{G}$, respectively, and where $x_{g,t}$ is the binary variable that represents the on-off status of generator g at time t .

The generator on-off status constraints are as follows:

$$x_{g,t} - x_{g,t-1} = su_{g,t} - sd_{g,t}, \quad (10)$$

where $su_{g,t}$ and $sd_{g,t}$ are the startup and shutdown binary variables of generator $g \in \mathcal{G}$ at time t , respectively.

The minimum startup and shutdown time duration constraints are as follows:

$$x_{g,t} \geq \sum_{\tau=T_g^{\text{on}}+1}^t su_{g,\tau}, \quad x_{g,t} \leq 1 - \sum_{\tau=t-T_g^{\text{off}}+1}^t sd_{g,\tau}, \quad (11)$$

where T_g^{on} and T_g^{off} are the minimum startup and shutdown time of generator $g \in \mathcal{G}$, respectively.

The ramping constraints are as follows:

$$P_{g,t}^{\mathcal{G}} - P_{g,t-1}^{\mathcal{G}} \leq R_g x_{g,t-1} + R_g^{\text{SU}} su_{g,t}, \\ P_{g,t-1}^{\mathcal{G}} - P_{g,t}^{\mathcal{G}} \leq R_g x_{g,t} + R_g^{\text{SD}} sd_{g,t}, \quad (12)$$

where R_g is the ramping limit of generator g . R_g^{SU} and R_g^{SD} are the startup capacity and shutdown capacity of generator $g \in \mathcal{G}$, respectively.

The power flow limits on transmission lines are as follows:

$$-\bar{P}_{ij} \leq P_{ij} \leq \bar{P}_{ij}, \quad \forall (i, j) \in \mathcal{B}, \quad (13)$$

where P_{ij} is the power flow on branch (i, j) and \bar{P}_{ij} is the corresponding upper bound of the transmission power flow.

For simplicity, the direct current power flow equation and the related power balance constraints are omitted here. The RoCoF constraints Eq. (7) and the COI frequency nadir constraints Eq. (8) are also included in the UC model.

The objective includes the conventional units' fuel costs and startup costs, as shown in Eq. (14). C_g^{op} and C_g^{st} are the operating and startup costs for units. C_i^{sto} is the operating cost for the primary regulation services of the energy storage devices.

$$\min \sum_{g \in \mathcal{G}, t \in \mathcal{T}} (C_g^{\text{op}} P_{g,t}^{\mathcal{G}} + C_g^{\text{st}} x_{g,t}) + \sum_{i \in \mathcal{L}, t \in \mathcal{T}} C_i^{\text{sto}} K_{i,t}. \quad (14)$$

The above-mentioned constraints and the objective formulate a unit-commitment problem. A year-round unit commitment problem is formulated when the time horizon \mathcal{T} is set as 8 760 hours. However, solving the 8 760-hour unit commitment model directly is time-consuming. We divide the 8 760 hours into several segments (four weeks per segment in this paper). Then, we add constraints to connect the end part of each segment to the start part of the next segment.

$$\sum_{t \in \mathcal{T}'} su_{g,t} = 0, \quad \sum_{t \in \mathcal{T}''} sd_{g,t} = 0, \quad (15)$$

where $\mathcal{T}' \subset \mathcal{T}$ represents the end part of each segment with length T^{bn} and $\mathcal{T}'' \subset \mathcal{T}$ represents the end part of each segment with length T^{bf} . The constraints ensure the continuity and consistency of the results. These two constraints do not restrict the hydro- and gas-fired units since they have no on-off time limits. Moreover, intraday startup/shutdown of thermal units is not frequent in the current power system. Therefore, the impacts of those constraints on the unit commitment results are limited.

2.4 Typical operation modes

In this work, we regard operation modes with the same conventional unit online condition (on/off status) as one typical operation mode. We denote the set of typical operation modes by \mathcal{S} , and the number of different typical operation modes is $|\mathcal{S}|$. In this way, we select the power load $P^{\mathcal{L}}$ and the corresponding $K_{i,t}$ at the same

time horizon among the operation modes as the typical values of one typical operation mode. To obtain all the typical operation modes, we solve the segmented year-round unit commitment problem formulated in Section 2.3, which is a preprocessing model.

3 Nodal frequency constraint generation

We require the nodal frequency nadirs of all buses to be above a threshold ω_{th} after any possible disturbance. This goal is realized through the proper placement of energy storage droop coefficients $K = [K_i]_{i \in \mathcal{L}}$ at different buses. This section aims to find a linear constraint to ensure that the droop coefficient placements of energy storage devices obey the frequency nadir restrictions.

In our previous research, the nodal frequency nadir constraints in a purely data-driven manner is built. For this approach, it is necessary to generate massive amounts of sampling data with different droop placement plans on typical online modes of conventional units. However, hundreds or even thousands of different online modes exist in year-round unit commitment results, and generating many samples for each mode is impossible. As a result, we introduce the idea of differential approximations for storage placements for efficient generation of effective nodal frequency constraints.

3.1 Nodal frequency response model

Figure 4 shows the nodal frequency response model after disturbances. The model considers the regulations of units and energy storage. Energy storage responds to nodal frequency deviations and provides primary regulations.

The swing equation with network considerations is shown in Eq. (16).

$$\frac{d}{dt} \begin{bmatrix} \theta_G \\ \omega_G \end{bmatrix} = \begin{bmatrix} 0 & \omega_0 I \\ -M^{-1}J & -M^{-1}\tilde{D} \end{bmatrix} \begin{bmatrix} \theta_G \\ \omega_G \end{bmatrix} + \begin{bmatrix} 0 \\ M^{-1}\Delta P \end{bmatrix}, \quad (16)$$

where θ_G is the rotor angle vector, ω_G is the corresponding frequency deviation vector, ω_0 is the line frequency (usually 100π or 120π rad/sec), $\tilde{D} = D - L\text{diag}(\mu)F$ is the damping coefficient matrix, $\Delta P = \Delta P^G - L\Delta P^L$ is the disturbance vector, and $J = B_{GG} - B_{GL}B_{LL}^{-1}B_{LG}$ is the Laplacian matrix. The load-side frequency deviation vector ω_L is calculated via the frequency divider formula $\omega_L = F\omega_G$, as discussed in Section 1.3. A detailed derivation can be found in Ref. [27]. Figure 5 shows an example of nodal frequency differences after disturbances.

3.2 Expressions of frequency nadir constraints

In this section, we derive a mathematical expression to link the amount of frequency nadir uplifting and the amount of energy storage placement (or droop coefficients equivalently).

In fact, we have given such an expression in the center-of-inertia research in Eq. (8). We rewrite it here in a detailed form.

$$\sum_{g \in \mathcal{G}} x_g A_{x_g} + K^{\text{coi}} A_K + P^{\mathcal{L}, \text{coi}} A_{P^L} + b \geq 0, \quad (17)$$

where A_{x_g} , A_K and A_{P^L} are the relative blocks of matrix A in Eq. (8), $K^{\text{coi}} = \mathbf{1}^T K$ is the summation of the droop coefficients, and $P^{\mathcal{L}, \text{coi}} = \mathbf{1}^T P^L$ is the summation of the load power injections. Based on the center-of-inertia constants, we derive the form of the unit

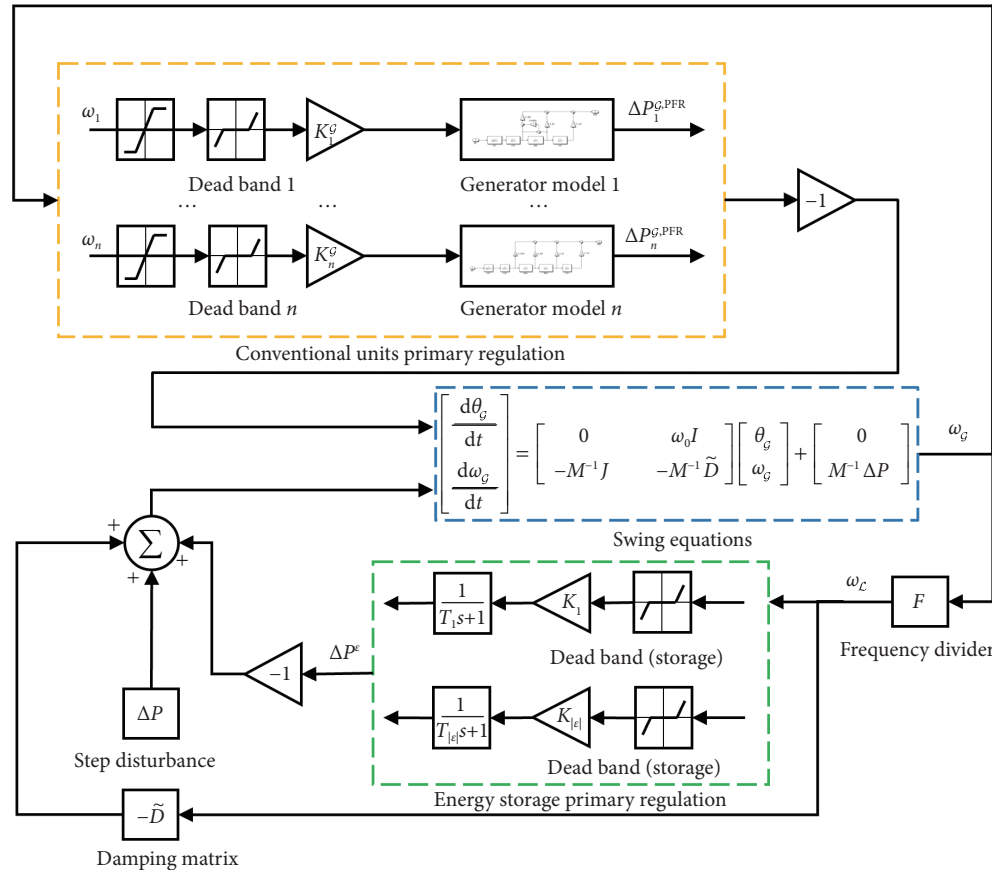


Figure 4 Nodal frequency response model.

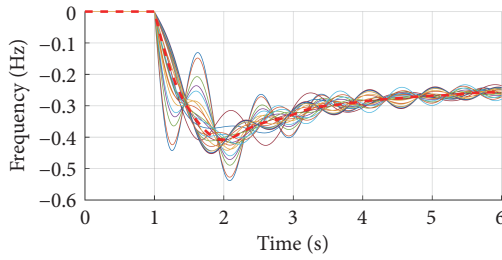


Figure 5 Nodal frequency variations in the modified RTS-79 case. The red dashed line is the COI frequency, and the other lines are nodal frequency records.

frequency nadir constraints.

First, for an online unit $g \in \mathcal{G}$, the corresponding form of Eq. (17) is shown in Eq. (18).

$$x_g A_{x_g} - e_g^T L K A_K - e_g^T L P^L A_{pL} + \tilde{b} \geq 0, \quad (18)$$

where e_g is a unit vector with only the g th element equal to one, L is the load power distribution matrix, and \tilde{b} is a constant vector.

Second, suppose there is an original droop placement plan $K^{(0)}$; we can verify whether the frequency nadir $\omega_g^{\text{nadir},(0)}$ satisfies the threshold ω_{th} . If not, we need to adjust the droop coefficients to lift its frequency nadir. Eq. (17) is rewritten into a differential form, as shown in Eq. (19).

$$x_g(1+\eta)\Delta A_{x_g} - e_g^T L(\Delta K)A_K - e_g^T L(\Delta P^L)A_{pL} \geq 0, \quad (19)$$

where $\Delta K = K - K^{(0)}$ represents the incremental droop coefficients and $\Delta P^L = P^L - P^{L,(0)}$ represents the incremental load power. ΔA_{x_g} is a coefficient related to the difference between the frequency nadir $\omega_g^{\text{nadir},(0)}$ and the threshold ω_{th} .

$$\Delta A_{x_g} = \frac{|\omega_g^{\text{nadir},(0)} - \omega_{\text{th}}|}{\omega_{\text{th}}} A_{x_g}. \quad (20)$$

The adjustment coefficient η is added to Eq. (19) to improve the accuracy of the constraints. The proper value of η is determined via an iterative process, which will be discussed in Section 3.3.

Third, we derive the form of nodal frequency constraints for typical operation modes (discussed in Section 2.4). Although ΔP^L is usually nonzero when we extend the constraints to periods with the same conventional unit online mode but different power loads, it can be neglected when we generate the constraints for a typical operating mode. The constraints for a typical operation mode are as follows:

$$-e_g^T L(\Delta K)A_K \geq -(1+\eta)\Delta A_{x_g}, \quad (21)$$

where $x_g = 1$ for online units. The constraints in Eq. (21) may be inaccurate because of the linear and differential assumptions. We refine the constraints through iterations in the following sections.

3.3 Constraint generation in local optimal solutions

We generate and refine the constraints for a typical operation mode. We assume that K^{coi} is evenly allocated to each bus, i.e., $K^{(0)} = K^{\text{coi}}/|\mathcal{N}|$, on buses in the initial placement plan. Here, $\eta = 0$.

We regenerate the constraints based on the simulation results of the initial plan via the method described in Section 3.2. Then, we solve a simple optimization problem to obtain local optimal solutions, as shown in Eq. (22). K^{max} is the maximum energy storage droop on buses.

$$\begin{aligned} \min \quad & 1^T K \\ \text{s.t.} \quad & 0 \leq K \leq K^{\text{max}} \\ & -e_g^T L(\Delta K)A_K \geq -(1+\eta)\Delta A_{x_g}, \quad \forall g \in \mathcal{G} \end{aligned} \quad (22)$$

The optimal solution of Eq. (22) is the new $K^{(0)}$, and we can refine the constraints iteratively. The iterative process ends when the global nodal frequency nadirs ($\min_{g \in \mathcal{G}} \omega_g^{\text{nadir}}$) during iteration are within a convergence threshold ω_{gap} , as shown in Eq. (23). ω_{gap} is set as 0.01 Hz in this paper. The threshold value is the same as the accuracy of common low-frequency-load-shedding protection equipment.

$$0 \leq \min_{g \in \mathcal{G}} \omega_g^{\text{nadir}} - \omega_{\text{th}} \leq \omega_{\text{gap}}. \quad (23)$$

When the nodal frequency nadir is above the threshold, i.e., $\min_{g \in \mathcal{G}} \omega_g^{\text{nadir}} - \omega_{\text{th}} > \omega_{\text{gap}}$, we can reduce the parameter η . For example, $\eta = \eta - 0.05$ for each iteration. Additionally, we can decrease the overall droop coefficient by reducing $K^{(0)}$. For example, $K^{(0)} = 0.8K^{(0)}$. In contrast, when the nodal frequency nadir is still below the threshold after several iterations, we can increase η , e.g., $\eta = \eta + 0.05$. An appropriate value must be chosen for the search rate for η . In this paper, 0.05 is an appropriate value and is selected for use in the algorithm. We verify that the algorithm converges well for both the RTS-79 and the 1089-bus test cases.

The workflow of the constraint generation and local optimal solutions is shown in Figure 6.

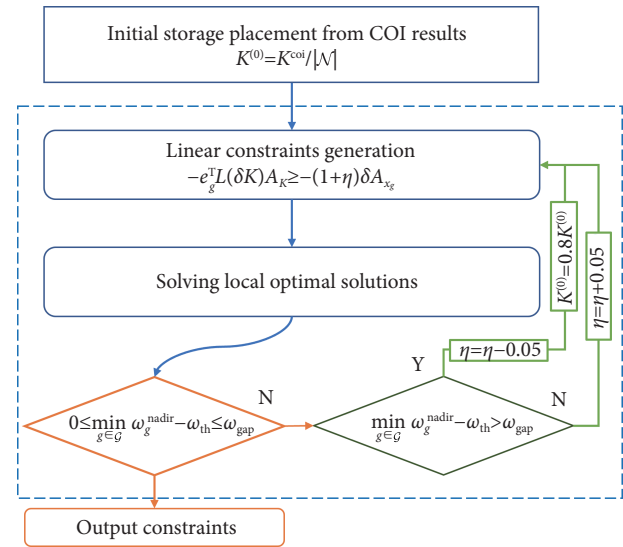


Figure 6 Workflow of the constraint generation and corrections.

3.4 Candidate locations for storage placements

An industrial power system can contain thousands of buses, and placing energy storage on every bus is unnecessary. Therefore, we may select some buses as candidates for energy storage placement.

In the previous section, we calculated the local optimal droop placement plans K for each typical operation mode. We denote K^s as corresponding to the s th typical operation mode. Then, we can calculate the weighted average values on buses based on the probabilities of the typical operation modes w .

$$K^{\text{ave}} = \sum_{s \in \mathcal{S}} w_s K^s \quad (24)$$

We choose the first N^{cand} buses of the sorted sequence K^{ave} as the candidates for energy storage placement.

3.5 Constraint corrections in global optimal solutions

In this section, we improve the accuracy of the generated constraints through a simplified planning model, as shown in Eq. (25). The optimization objective is a simplification of Eq. (31), which represents the final energy storage planning problem. C_i^{inv} is the energy storage investment cost, and C_i^{sto} is the operational cost corresponding to the frequency services. Energy storage reserves its capacity for primary regulations, and its operation cost is tiny compared with that of investment. Eq. (25) also includes all the constraints generated from Eq. (22).

$$\begin{aligned} & \min \sum_{i \in \mathcal{L}} C_i^{\text{inv}} \omega_{\text{th}} K_i + \sum_{i \in \mathcal{L}, t \in \mathcal{T}} C_i^{\text{sto}} \tilde{K}_{i,t} \\ & \text{s.t., } \tilde{K}_{i,t} \leq K_i \leq K_i^{\text{max}}, \forall i \in \mathcal{L}, t \in \mathcal{T} \\ & \text{Inequality (21), } \forall t \in \mathcal{T}, s \in \mathcal{S} \end{aligned} \quad (25)$$

Then, we regenerate the constraints according to the results in Eq. (25). We use the $\tilde{K}_{i,t}$ solved from Eq. (25) as the initial values for constraint generation with the method described in Section 3.3. The accuracy of the constraints may be improved through multiple iterations, i.e., simplified planning and constraint generation.

4 Energy storage planning considering COI and nodal frequency constraints

4.1 Energy storage model

Energy storage has three major functions: primary frequency regulation against disturbances, secondary regulation, and peak shaving. We perform energy storage planning considering all three functions based on the year-round unit commitment results.

The energy storage maximum power capacity, state of charge (SoC), maximum SOC, and charge/discharge power on each bus are defined as $P^{\text{sto,max}}$, E , E^{max} , P^{cha} , and P^{dis} , respectively. The charge/discharge efficiency is ξ . Additionally, we control the SoC within the range of [0.1, 0.9] to reduce electrothermal aging^[29]. It is the most common energy storage system manufactured and operated in China. The general model of energy storage is shown in Eqs. (26) and (27).

$$0.1E^{\text{max}} \leq E_t \leq 0.9E^{\text{max}}, \forall t \in \mathcal{T} \quad (26)$$

$$E_{t+1} = E_t + \zeta P_t^{\text{cha}} - \zeta^{-1} P_t^{\text{dis}}, \forall t \in \mathcal{T}. \quad (27)$$

Energy storage provides primary frequency regulation (PFR) to support stability after disturbances.

Therefore, there should be at least $P^{\text{PFR}} = \omega_{\text{th}} K$ power reserves in energy storage systems for primary regulations.

Energy storage also provides fast secondary frequency regulation (SFR) to offset short-term renewable fluctuations. We set the power reserves as 20% of the short-time fluctuations. The magnitude of the fluctuations is 10% of the renewable outputs, as discussed in Ref. [6]. In summary, we need to keep at least $P^{\text{SFR}} = 0.02P^{\mathcal{R}}$ power reserves for secondary regulations. $P^{\mathcal{R}}$ is the renewable power output.

Furthermore, energy storage realizes peak shaving through charging and discharging, i.e., P^{cha} and P^{dis} . We assume that the storage SoC is 20% of the maximum at the start of every day, as shown in Eq. (28).

$$E_t = 0.2E^{\text{max}}, \text{ for all } t \in \mathcal{T} \text{ that divides } 24. \quad (28)$$

The correlations among primary frequency regulation, secondary frequency regulation, and peak shaving power are shown in Eqs. (29) and (30).

$$0 \leq P^{\text{PFR}} \leq P^{\text{sto,max}} - P^{\text{SFR}} - (P^{\text{dis}} - P^{\text{cha}}), \quad (29)$$

$$0 \leq P^{\text{SFR}} \leq P^{\text{sto,max}} - |P^{\text{dis}} - P^{\text{cha}}|. \quad (30)$$

4.2 Energy storage planning

We determine both the locations of the energy storage systems and their power capacity $P^{\text{sto,max}}$ by solving the year-round planning problem. The online modes and power outputs are generally based on the year-round unit commitment results following the COI frequency constraints. As a result, we can fix all binary variables in Eqs. (9)–(13), and the planning model becomes a pure linear programming optimization problem.

$$\min \sum_{i \in \mathcal{E}} C_i^{\text{inv}} P_i^{\text{sto,max}} + \sum_{t=1}^{8760} \sum_{i \in \mathcal{E}} C_i^{\text{sto}} \tilde{K}_{i,t} \quad (31)$$

The optimization objective of the planning model is shown in Eq. (31). The dominant item $\sum_{i \in \mathcal{E}} C_i^{\text{inv}} P_i^{\text{sto,max}}$ represents the investment costs. C_i^{inv} is the annual investment cost. The second term $\sum_{t=1}^{8760} \sum_{i \in \mathcal{E}} C_i^{\text{sto}} \tilde{K}_{i,t}$ minimizes the energy storage droop coefficients.

The primary constraints in the planning models include the energy storage constraints Eqs. (26)–(30), the frequency security constraints Eqs. (7) and (8) and (21), the operational constraints Eqs. (9)–(13), and the power balance Eq. (32).

$$\sum_{i \in \mathcal{G}} P_{i,t}^{\mathcal{G}} + \sum_{i \in \mathcal{R}} P_{i,t}^{\mathcal{R}} + \sum_{i \in \mathcal{H}} P_{i,t}^{\mathcal{H}} + \sum_{i \in \mathcal{E}} (P_{i,t}^{\text{cha}} - P_{i,t}^{\text{dis}}) = \sum_{i \in \mathcal{L}} P_{i,t}^{\mathcal{C}}. \quad (32)$$

5 Case studies

Two test cases are studied to verify the effectiveness of the proposed approach, namely, a modified 24-bus RTS-79 power system and a 1089-bus practical power system in Jiangsu Province, China. The RTS-79 case is a widely used test case in related research, and the Jiangsu case aims to demonstrate the scalability of the proposed approach. We select eight types of conventional units in the test cases, including primary reheat units (TB3, TB6, TB10), secondary reheat units (TC6, TC10), a hydroturbine (GH3), and gas-fired units (TG3, TG6)^[28,30]. The labels 3, 6, and 10 represent 300, 660, and 1000 MW units, respectively. Furthermore, we add small random disturbances to the typical units' parameters such that every unit is different from others in the test cases. The potential power disturbances are set as the operating power of the HVDC lines because HVDC failures are common failures in practical operations and can severely influence system frequency security. Our planning model needs to reserve enough margin of frequency regulation to prevent the system from violating the frequency security requirements for all time horizons under these potential power disturbances.

The codes used for the work described in this section are implemented in Python 3.10 and MATLAB R2022b. The optimization problems are solved via Gurobi 10.0. The simulation models are built in MATLAB-Simulink. The computation is performed on an AMD-RT-5950X CPU.

5.1 A modified RTS-79 test case

There are 24 buses and 33 conventional units in the RTS-79

case^[31]. The maximum power load, solar output, and wind power output are 15 GW, 5 GW, and 3 GW, respectively. Two HVDCs are injected into the grid at Bus 4 and Bus 19. The power injections of each HVDC are 1.2 GW from 7 a.m. to 9 p.m. and 0.8 GW in other periods. Twelve TB3, thirteen TB6, two TC6, four TG3, and two GH3 units are installed in the system. The frequency nadir threshold for each bus is set as 49.50 Hz, and that for the COI is set as 49.55 Hz. There are 75 typical operation modes obtained by the preprocessing model in Section 2.3.

Table 1 shows the installation plan for energy storage systems. The results are reasonable and understandable. The northern part (Bus 13 to Bus 23) of the RTS-79 case has more synchronous generators than the southern part does (Bus 1 to Bus 12, Bus 24). Therefore, the total energy storage capacity in the northern part is higher than that in the southern part. Since Bus 2 is the closest generation-side bus to the possible HVDC disturbance at Bus 4, the generator on Bus 2 may confront severe active power imbalances when the HVDC fails. As a result, 179 MW of energy storage is planned here. On the other hand, the energy storage installations are much more uniform near the other possible HVDC disturbance point, i.e., Bus 19; this is because six synchronous generators are located near Bus 19, and the possible active power imbalances are less severe than those near Bus 4. In addition, the capacity of energy storage is set as a continuous value in the planning model. For real-world applications, the energy storage capacity should be rounded to the nearest suitable value. For example, the 0.1 MW energy storage planned at bus 1 may be rounded to zero in practical applications.

Table 1 Planning results of the energy storage capacity (MW)

| Bus | Capacity | Bus | Capacity | Bus | Capacity |
|-----|----------|-----|----------|-----|----------|
| 01 | 0.1 | 09 | 1.0 | 17 | 13.4 |
| 02 | 179.1 | 10 | 0.5 | 18 | 11.4 |
| 03 | 0.4 | 11 | 1.4 | 19 | 20.4 |
| 04 | 1.4 | 12 | 1.4 | 20 | 19.7 |
| 05 | 0.2 | 13 | 37.8 | 21 | 12.3 |
| 06 | 0.7 | 14 | 2.3 | 22 | 11.8 |
| 07 | 39.6 | 15 | 26.6 | 23 | 19.0 |
| 08 | 1.4 | 16 | 23.4 | 24 | 1.0 |

A comparison is conducted to illustrate the improvement of the planned energy storage. After solving the optimization problem, we perform a nodal frequency dynamics simulation (as introduced in Section 3.1) for every operating state under the disturbances of HVDC failures. The simulation results suggest that planned energy storage can effectively improve the system's frequency security because the nodal frequency nadirs after these disturbances are all lifted above the threshold. Figure 7 shows one such result. The red line represents the nodal frequency dynamics with our planned energy storage devices, and the blue line represents the dynamics without these planned energy storage devices. Therefore, the contribution of planned energy storage to improving frequency dynamics can be clearly visualized. For clarity, only the nodal frequency dynamics of Bus 7 are shown. The nodal frequency nadir is below the threshold without planned energy storage, whereas it satisfies the threshold with planned energy storage. The two curves indicate that the nodal frequency nadir is significantly improved upon the placement of energy storage. In addition, the final value of the nodal frequency is also improved.

Figure 8 illustrates the SoC and the reserves for primary fre-

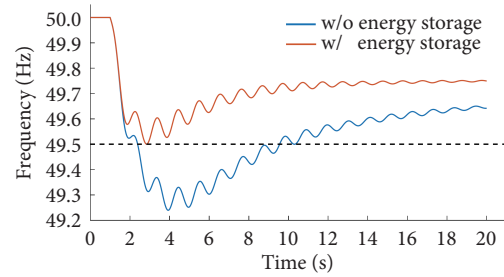


Figure 7 Comparison of nodal frequency dynamics after a 1.2 GW disturbance located at Bus 19. The red line represents the dynamics with our planned energy storage devices, and the blue line represents the dynamics without these energy storage devices. For clarity, only the nodal frequency dynamics of Bus 7 are shown.

quency regulation of the planned energy storage systems throughout a typical day. The figure reveals that the reserves for primary frequency regulation are higher between 7 a.m. and 9 p.m. than they are in other periods. This is closely linked to the HVDC injections, which are 1.2 GW from 7 a.m. to 9 p.m. and 0.8 GW from 10 p.m. to 6 a.m. the following day. In the event of an HVDC failure, the system experiences significant active power imbalances. The larger reserve of primary frequency regulation during the 7 a.m. to 9 p.m. period is due to the greater potential for active power imbalances at this time. Additionally, Figure 8 demonstrates a cooperative relationship between the SoC and primary frequency regulation reserves. To provide adequate power and energy support when primary frequency regulation is needed, energy storage systems tend to reserve more SoC during periods of higher demand for primary frequency regulations.

Energy storage can provide primary regulation services, secondary regulation services, and peak shaving services. Figure 9 shows a histogram of the energy storage power capacity utilization ratios. The histogram shows that primary regulation services and peak shaving services usually involve less power than secondary

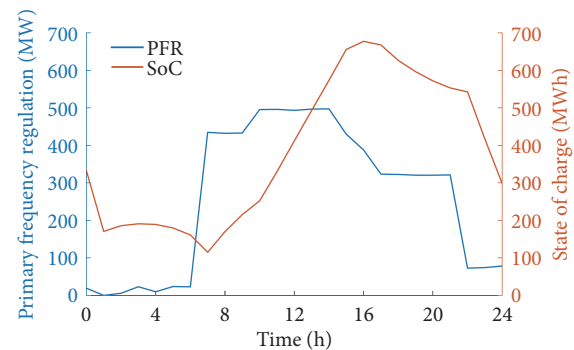


Figure 8 SoC and the reserved primary frequency regulations of the planned energy storage systems during a typical day.

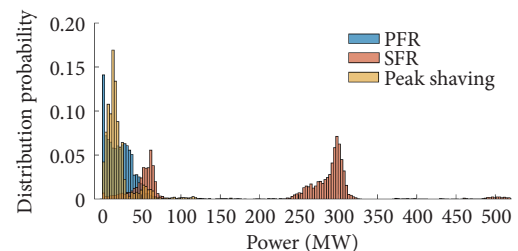


Figure 9 Histogram of the energy storage power capacity utilization ratios in the RTS-79 case.

regulation services do. This is also consistent with practical operations.

5.2 A practical power system in Jiangsu Province, China

There are 1089 buses and 317 conventional units in the Jiangsu case. Jiangsu contains thirteen cities—Nanjing (NJ), Wuxi (WX), Xuzhou (XZ), Changzhou (CZ), Suzhou (SZ), Nantong (NT), Lianyungang (LY), Huaian (HA), Yancheng (YC), Yangzhou (YZ), Zhenjiang (ZJ), Taizhou (TZ), and Suqian (SQ)—which are shown in Figure 10. Owing to data policy restrictions of the State Grid Corporation of China, only substations above 500 kV are shown in the figure. The typical power flow directions are labeled with arrows. The maximum power load is approximately 135 GW, and the total installed capacity of the renewable energy is approximately 90 GW. Additionally, four HVDC injections carry green power from inland China to Jiangsu. Two HVDCs are located in SZ, one in NJ, and one in TZ. The power injections of each HVDC are set to 4 GW from 7 a.m. to 9 p.m. and to 3 GW in other periods. Nighty-five TB3, forty-five TB6, five TC6, thirty-two TB10, twelve TC10, ninety-one TG3, twenty-four GH3, and thirteen TG6 units are installed in the power systems. The frequency nadir threshold for each bus is set as 49.75 Hz, and that for the COI is set as 49.8 Hz. Eighty buses are selected as candidates for energy storage placements. There are 3994 typical operation modes obtained by the preprocessing model in Section 2.3.

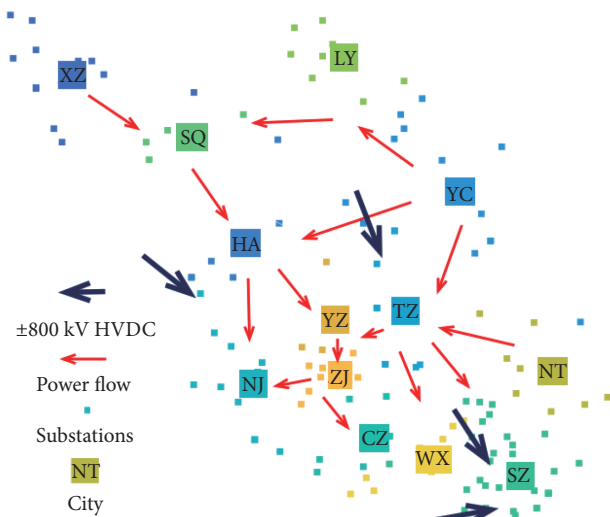


Figure 10 Typical power flow directions and substations above 500 kV in Jiangsu. The text in boxes shows a city's position, depicting buses in the same color. The dark blue arrows are ± 800 kV HVDC injections.

The optimal energy storage placement results are shown in Figure 11. For clarity, the storage installations are summarized in cities. The energy storage systems are mainly placed in SZ, NJ, and TZ, where the HVDC injections are located. The total capacity of the energy storage systems to be installed is 4189 MW. The energy storage systems in SZ account for more than 29.7% of the total capacity, and those in NJ and TZ account for 12.6% and 10.8%, respectively. The top three cities account for 53.1% of the total capacity, which is larger than one half of the total capacity. The numerical results are consistent with the characteristics of the practical power system since the HVDC terminals are located in the three cities. HVDC terminals may reduce their neighbors' grid strength, introduce potentially significant power disturbances, and increase the possibility of frequency insecurity.

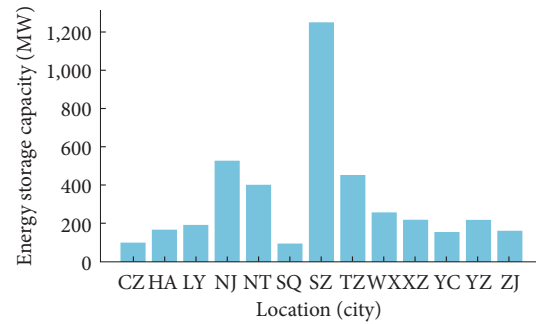


Figure 11 Storage planning results in the Jiangsu case. For clarity, storage installations are summarized in cities.

Finally, we verify the efficiency and effectiveness of our methods in this large-scale case. Our method takes only 19.5 minutes to solve the year-round 8760-hour placement problem for a system of over 1000 buses and 300 generators. Based on the planning results, we perform a nodal frequency dynamics simulation for every operating state under the disturbances of HVDC failures. The nodal nadirs are above 49.75 Hz for all periods. The COI nadirs are above 49.8 Hz in 95.4% of the periods. Figure 12 shows the probability distributions of the remaining 4.6% violations of the COI frequency nadirs. The probability histogram shows that the maximum violation is 0.000387 Hz, which can be neglected in practice.

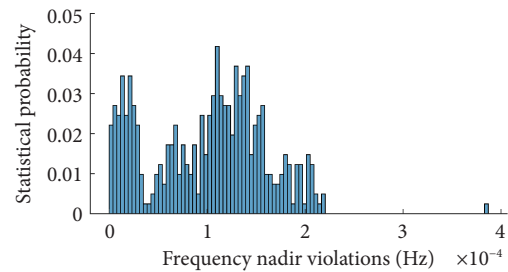


Figure 12 Probability histogram of the 4.6% violations of the COI frequency nadirs in the Jiangsu case.

5.3 Performance discussion

We discuss two aspects of our methods' performance, i.e., efficiency and effectiveness.

First, we compare our nodal frequency constrained energy storage planning model with a traditional energy storage planning model. For clarity, we specify the two models as follows. The two models have the same objective, Eq. (31). The traditional model consists of energy storage constraints Eqs. (26)–(30), synchronous generator constraints Eqs. (9)–(13), and power balance constraints Eq. (32). Our planning model consists of energy storage constraints Eqs. (26)–(30), synchronous generator constraints Eqs. (9)–(13), power balance constraints Eq. (32), center-of-inertia frequency security constraints Eqs. (7) and (8), and nodal frequency security constraints Eq. (21), where binary variables have been fixed according to their operation modes. Specifically, before solving our planning model, we have several preprocessing steps, as described in Section 2.3. We set the same optimality gap of 1% for both models and a 6-hour time limit for the solver. For the RTS-79 case, our planning model only takes 221 seconds to solve the 8760-hour problem, and the preprocessing steps take 10.03 minutes. However, the traditional model exceeds the 6-hour time limit and only reaches a 2.2% optimality gap. The results suggest that our planning model lowers the computational burden and

improves efficiency. One important reason is that we formulate the nodal frequency constrained energy storage planning model as a pure linear programming optimization problem.

Second, we validate our methods' effectiveness by analyzing our preprocessing model in Section 2.3. As discussed above, the primary assumption of our methods lies in the preprocessing model. We verify the accuracy of the segmented preprocessing model with respect to the original model. For the RTS-79 case, the objective values of the two models are 0.05% different, which is very small and acceptable in practice. The numerical results suggest that our preprocessing model closely approximates the original model. Our segmented model takes 10.03 minutes, whereas the original model takes 80.59 minutes. The benefits of our methods are significant, especially for large-scale systems.

6 Conclusions and future work

This paper proposes an energy storage planning method that considers the COI and nodal frequency constraints. First, we obtain year-round operation modes through a COI frequency-constrained unit commitment model and generate nodal frequency constraints for all modes. The energy storage is then planned with COI and nodal frequency constraints in both capacities and locations. Finally, we verify the method in a modified RTS-79 system and practical large-scale cases. The main conclusions include the following: (1) Our method guarantees both COI and nodal frequency limits in year-round operation modes. (2) Energy storage is prone to be placed near disturbances. (3) The method is suitable for large-scale systems.

For future work, we will consider reducing the number of operating modes by clustering when generating nodal frequency constraints. Additionally, the power system stabilizer and detailed power electronic models can be added to the simulations.

Acknowledgements

This work was supported in part by the National Natural Science Foundation of China (No. 52177093) and in part by the Scientific & technical project of China Electric Power Planning & Engineering Institute (K202317).

Article history

Received: 20 December 2024; Revised: 10 February 2025; Accepted: 24 February 2025

Additional information

© 2025 The Author(s). This is an open access article under the CC BY license (<http://creativecommons.org/licenses/by/4.0/>).

Declaration of competing interest

The authors have no competing interests to declare that are relevant to the content of this article.

References

- [1] Kalair, A., Abas, N., Khan, N. (2016). Comparative study of HVAC and HVDC transmission systems. *Renewable and Sustainable Energy Reviews*, 59: 1653–1675.
- [2] Welcome to State Grid Corporation of China. (2024). Available at <http://www.sgcc.com.cn/>
- [3] Global Times (2021). China's state grid: Linking north and south of

- Brazil. Available at <https://www.globaltimes.cn/page/202108/1232633.shtml>
- [4] Niu, D., Fang, J., Yau, W., Goetz, S. M. (2023). Comprehensive evaluation of energy storage systems for inertia emulation and frequency regulation improvement. *Energy Reports*, 9: 2566–2576.
- [5] Liang, J., Fan, H., Cheng, L., Rong, S., Li, T., Yu, T., Wang, L. (2024). Control strategy for improving the frequency response characteristics of photovoltaic and energy storage systems based on VSG control. *Energy Reports*, 11: 2295–2305.
- [6] Zhang, J., Zhang, N., Ge, Y. (2023). Energy storage placements for renewable energy fluctuations: A practical study. *IEEE Transactions on Power Systems*, 38: 4916–4927.
- [7] Liu, Y., He, Q., Shi, X., Zhang, Q., An, X. (2023). Energy storage in China: Development progress and business model. *Journal of Energy Storage*, 72: 108240.
- [8] Teng, F., Trovato, V., Strbac, G. (2016). Stochastic scheduling with inertia-dependent fast frequency response requirements. *IEEE Transactions on Power Systems*, 31: 1557–1566.
- [9] Badesa, L., Teng, F., Strbac, G. (2020). Pricing inertia and frequency response with diverse dynamics in a mixed-integer second-order cone programming formulation. *Applied Energy*, 260: 114334.
- [10] Zhang, Z., Du, E., Teng, F., Zhang, N., Kang, C. (2020). Modeling frequency dynamics in unit commitment with a high share of renewable energy. *IEEE Transactions on Power Systems*, 35: 4383–4395.
- [11] Li, K., Guo, H., Fang, X., Liu, S., Teng, F., Chen, Q. (2023). Market mechanism design of inertia and primary frequency response with consideration of energy market. *IEEE Transactions on Power Systems*, 38: 5701–5713.
- [12] Shen, Y., Wu, W., Wang, B., Yang, Y., Lin, Y. (2023). Data-driven convexification for frequency nadir constraint of unit commitment. *Journal of Modern Power Systems and Clean Energy*, 11: 1711–1717.
- [13] Lagos, D. T., Hatziaargyriou, N. D. (2021). Data-driven frequency dynamic unit commitment for island systems with high RES penetration. *IEEE Transactions on Power Systems*, 36: 4699–4711.
- [14] Zhang, J., Jia, H., Zhang, N. (2023). Alternate support vector machine decision trees for power systems rule extractions. *IEEE Transactions on Power Systems*, 38: 980–983.
- [15] Zhang, Y., Cui, H., Liu, J., Qiu, F., Hong, T., Yao, R., Li, F. (2022). Encoding frequency constraints in preventive unit commitment using deep learning with region-of-interest active sampling. *IEEE Transactions on Power Systems*, 37: 1942–1955.
- [16] Zhang, Y., Chen, C., Liu, G., Hong, T., Qiu, F. (2021). Approximating trajectory constraints with machine learning—microgrid islanding with frequency constraints. *IEEE Transactions on Power Systems*, 36: 1239–1249.
- [17] Ørum, E., Kuivaniemi, M., Laasonen, M., Bruseth, A. I., Jansson, E. A., Danell, A., Elkington, K., Modig, N. (2015). Future system inertia. Nordic Report. ENTSOE. Available at https://eepublicdownloads.entsoe.eu/clean-documents/Publications/SOC/Nordic/Nordic_report_Future_System_Inertia.pdf
- [18] Badesa, L., Teng, F., Strbac, G. (2021). Conditions for regional frequency stability in power system scheduling: Part I: Theory. *IEEE Transactions on Power Systems*, 36: 5558–5566.
- [19] Poolla, B. K., Bolognani, S., Dörfler, F. (2017). Optimal placement of virtual inertia in power grids. *IEEE Transactions on Automatic Control*, 62: 6209–6220.
- [20] Milano, F., Ortega, Á. (2017). Frequency divider. *IEEE Transactions on Power Systems*, 32: 1493–1501.
- [21] Zhao, J., Mili, L., Milano, F. (2018). Robust frequency divider for power system online monitoring and control. *IEEE Transactions on Power Systems*, 33: 4414–4423.
- [22] Hou, Q., Du, E., Zhang, N., Kang, C. (2020). Impact of high renewable penetration on the power system operation mode: A data-driven approach. *IEEE Transactions on Power Systems*, 35: 731–741.
- [23] Du, E., Zhang, N., Kang, C., Xia, Q. (2019). A high-efficiency network-constrained clustered unit commitment model for power system

- planning studies. *IEEE Transactions on Power Systems*, 34: 2498–2508.
- [24] Zhang, N., Jiang, H., Du, E., Zhuo, Z., Wang, P., Wang, Z., Zhang, Y. (2022). An efficient power system planning model considering year-round hourly operation simulation. *IEEE Transactions on Power Systems*, 37: 4925–4935.
- [25] Meus, J., Poncelet, K., Delarue, E. (2018). Applicability of a clustered unit commitment model in power system modeling. *IEEE Transactions on Power Systems*, 33: 2195–2204.
- [26] Tejada-Arango, D. A., Domeshek, M., Wogrin, S., Centeno, E. (2018). Enhanced representative days and system states modeling for energy storage investment analysis. *IEEE Transactions on Power Systems*, 33: 6534–6544.
- [27] Wang, J., Zhang, J., Hou, Q., Jiang, H., Strbac, G., Teng, F., Zhang, N. (2025). Analytical decomposition of nodal frequency responses. *IEEE Transactions on Power Systems*, 40: 1176–1179.
- [28] China Electric Power Research Institute (2015). PSD-BPA Transient Stability Program User Manual 5th Ed.
- [29] Li, Y., Gu, Y., He, G., Chen, Q. (2023). Optimal dispatch of battery energy storage in distribution network considering electrothermal-aging coupling. *IEEE Transactions on Smart Grid*, 14: 3744–3758.
- [30] China Power Engineering Consulting Group Co., Ltd. (2019). *Power Engineering Design Manual: Power System Planning and Design*. China: China Electric Power Press.
- [31] Zimmerman, R. D., Murillo-Sánchez, C. E., Thomas, R. J. (2011). MATPOWER: Steady-state operations, planning, and analysis tools for power systems research and education. *IEEE Transactions on Power Systems*, 26: 12–19.